Contents lists available at ScienceDirect

NDT&E International

Tomographic reconstruction for concrete using attenuation of ultrasound

H.K. Chai [a,*], S. Momoki [a], Y. Kobayashi [b], D.G. Aggelis [c], T. Shiotani [d]

[a] Research Institute of Technology, Tobishima Corporation, 5472 Kimagase, Noda, Chiba 270-0222, Japan
[b] College of Science and Technology, Nihon University, 8-14, Kanda-Surugadai 1-chome, Chiyoda-ku, Tokyo 101-8308, Japan
[c] Department of Materials Science and Engineering, University of Ioannina, Ioannina 45110, Greece
[d] Graduate School of Engineering, Kyoto University, C1-2-236, Kyoto-Daigaku-Katsura, Nishikyo-Ku, Kyoto 615-8540, Japan

ARTICLE INFO

ABSTRACT

The development of attenuation tomography for concrete is discussed. Fundamental ultrasonic measurements of cubic specimens and numerical simulations of wave motion were conducted to examine the decay in amplitude of ultrasound when impinged by defect, and compare its sensitivity to the delay in travel time. An algorithm was then developed to facilitate simultaneous tracing and distribution of amplitude factor in a three-dimensional model by iterative computation. The algorithm was used for reconstruction of attenuation tomographic for visualizing concrete interior. Experimental results indicated successful identification for the location of a defect that was embedded in concrete, thus implying the potential of attenuation tomography as a complementary method to the travel time tomography to enhance soundness evaluation of concrete.

© 2010 Elsevier Ltd. All rights reserved.

1. Introduction

Tomography is an emerging technique for non-destructive evaluation of concrete. The objective of tomography is to provide visualization, either by cross section or three dimensional structure of the structure interior, so that better identification of anomalous regions and determination of physical properties of the measured region can be achieved [1]. The advantage is that the results combine information from several interconnected travel paths, minimizing therefore, the possibility of missing defects due to unfavourable orientation or small size. Additionally, the final results supplied in the form of tomograms are readily available for the user (engineer, owner of structure) to interpret without need of specialized analysis.

The X-ray computed tomography, a well established tool for medical purposes, has demonstrated highly promising implementation for characterizing concrete constituents in the laboratory scale to enable reliable numerical study on the influence of different crack formations and air void scattering inside concrete on wave propagation [2]. Report is also found regarding effective utilization of the technique for quantifying freeze and thaw damage of concrete core specimens [3]. In terms of in-situ application, the travel-time tomography has been widely applied. This technique shares similar concept with the common seismic tomography adopted for geophysical studies [4–6], in which the arrival times of body waves,

(usually of primary, P-waves), from multiple ray paths are observed, collected and then used as input for computing the distribution of wave velocity in association with each ray path within the meshed model [7]. The process is an inverse one because it reconstructs the interior of the object based on information obtained from the projections by algebraic methods. The major drawback of the inversion process is its high computational cost. However, with recent advancement in computer technology, the relevant constraints become almost ineligible even for large-scale application.

The travel-time tomography has been effectively adopted for various types of concrete structures. These include evaluation of grouted post-tensioned bridge beams [8], assessment of solidification of a newly constructed concrete bridge pier cap [9] as well as aging mass concrete dam [10]. Successful implementation was also achieved for evaluating the repair of structures, i.e. by comparing the velocity structures before and after repair of a bridge deck cross section containing a through-the-thickness crack [11]. Besides, there were separate reports on examining the velocity change of cracked concrete piers of an aging water intake facility due to filling by cementitious material [12–14], and to justify the eventual increase of velocity after hardening of the filler [15].

Besides travel time, attenuation of elastic waves is also utilized for tomographic reconstruction. It was stated that attenuation is vital for characterizing properties of rock and fluid because attenuation is more sensitive than velocity to some of the material condition properties, such as saturation, porosity, permeability and viscosity [16]. In this type of geophysical exploration, however, the attenuation nature of waves, which are usually generated from low frequency impact and possess wavelengths possibly much greater

* Corresponding author. Tel.: +81 4 7198 7559; fax: +81 4 7198 7586.
E-mail address: hwakian.chai@gmail.com (H.K. Chai).

than the scale of target structure, varied from that observed in concrete.

Attenuation of waves, which is represented by the decrease in wave amplitude due to reduced propagation energy, is usually caused by both intrinsic properties of material and geometrical spreading. Amplitude decay can also happen if the wave is impinged by an anomaly, a phenomenon commonly known as scattering attenuation. Several sources in literature have discussed on the development and adoption of different tomography techniques employing scattering attenuation for geophysical prospecting. For example, a specific study utilized the change in near-surface seismic wave amplitude for tomography reconstruction [17]. To improve accuracy of the attenuation tomography technique, the shift of frequency of waves due to object inhomogeneity was examined and used as tomography input [18]. Although the frequency shift method appears to be more robust than the amplitude decay method, data interpretation involves an indirect, slightly more complicated approach. In addition, it is essential that the recorded data be broad band so that the frequency shift can be estimated easily. Reports on practical applications of attenuation tomography for concrete structures seem limited. A most recent one stated that the use of frequency shift method for inspection of solidification of pier cap of a reinforced concrete bridge pier cap, in complement to the travel time tomography technique [9]. Besides, there is an experimental study that compared attenuation tomography and velocity tomography for detecting concrete inhomogeneity in the forms of a void and a region filled with mortar, respectively [19]. In this study, a two-dimensional ray-trace algorithm was used for inversion of amplitude obtained from the first arriving ultrasonic waves, which yielded enhanced visualizations for the concrete interior and demonstrated the superiority of the technique.

Considering differences with regards to scale, geometrical complexity and intrinsic material inhomogeneity of concrete structures compared to soils or rocks on which tomography techniques are more commonly applied, studies are still necessary for enhancing the reliability of the techniques. In this current study, the authors first carried out numerical simulations of wave motion to investigate the attenuation behaviour of ultrasound in concrete with inhomogeneity. Then the feasibility of utilizing amplitude decay of ultrasound for visualizing defect inside a concrete specimen was examined through the attenuation tomography technique. The attenuation tomography technique employs a ray-trace algorithm that facilitates the use of general purpose finite element pre-processor for model meshing, thus greatly enhances the flexibility of measurement and analysis as well as reduces operational cost. One key feature of the three dimensional visualization is that with the use of an appropriate graphical application for generating contour output, e.g. graphical post-processor for finite element analysis, visualization of any two-dimensional segment within the measurement perimeter can be performed.

2. Attenuation of ultrasound in heterogeneous concrete

Simple through-transmission measurement was carried out in an earlier work to examine the influence of concrete inhomogeneity on attenuation of ultrasound [20]. Mortar cubic specimens of 150 mm side were prepared for the purpose. In order to simulate damage, different volume percentages of thin vinyl plates were included in the specimens, namely 0%, 1%, 5% and 10%. The dimensions of the flaky inclusions were $15 \times 15 \times 0.5$ mm^3 and their acoustic impedance was much lower than that of concrete. The experimental set-up is shown in Fig. 1. Ultrasonic pulse with a central frequency of approximately 110 kHz was excited using a pulse generator (PAC H-101CV). For recording incident and transmitted waveforms, AE sensors with a 60 kHz resonant frequency (PAC R6) were adopted. The collected data was analyzed for transit
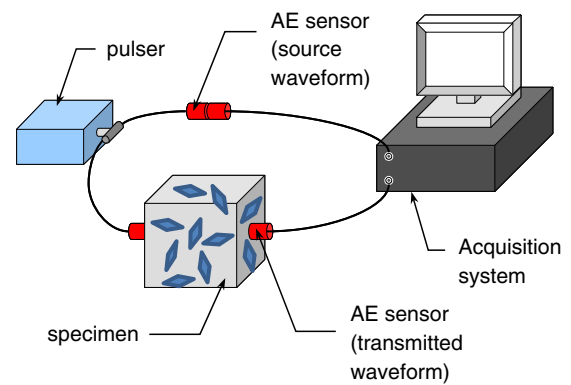

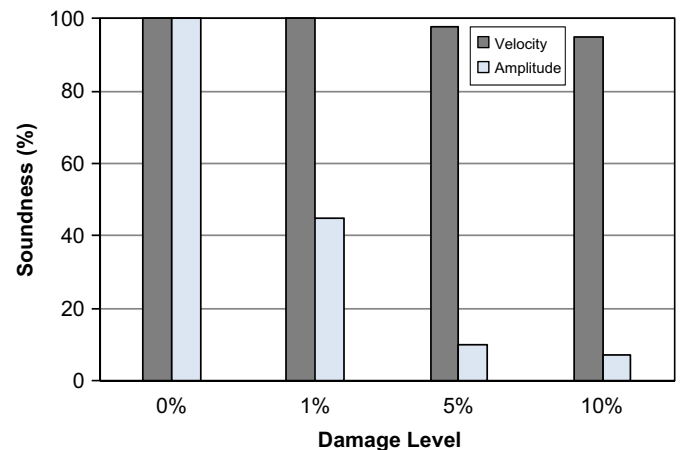Fig. 1. Experimental setup for measuring concrete cube with vinyl plate inclusions.

Fig. 2. Soundness evaluation by change of velocity and amplitude with regards to damage level.

time from the source to receiver in order to compute propagation velocity; as well as to quantify attenuation by dividing the maximum absolute amplitude of the receiving waveform with that of the source waveform. Fig. 2 presents the results of both measurements, plotted as percentage of the corresponding values in plain material (0% inclusions) versus the inclusion content. The values obtained for the plain material are assumed to indicate sound material, thus 100% on the soundness scale. It can be noticed that, while the indicated decrease in soundness by velocity change was not pronounced even for the 10% damage level (up to 11% decrease), the soundness as evaluated by amplitude change has recorded a decrease by more than 90% for the similar damage level. The results in general indicated that quantitative evaluation of concrete damage can be better performed using amplitude than velocity as the measured parameter.

In order to take advantage of the characterization power of wave amplitude, attenuation tomography was experimentally applied in a concrete specimen with a large embedded Styrofoam plate, with the results of some preliminary numerical simulations, which will be discussed below, serving as a guide.

3. Principle of travel-time and attenuation tomography techniques

In travel-time tomography, the travel time of wave along a path is used as the observed data and the slowness (the inverse of wave velocity) is employed as the computed property of the measured object. To resolve the inverse problem of estimating the object

property using the observed data, a ray-tracing technique is commonly applied. In SIRT (Simultaneous Iterative Reconstruction Technique)-based ray-trace methodology [21], propagation of wave is based on Hyugen's principle in a two dimensional space subdivided into square cells. The length, l_j, of a ray-path is obtained by directly computing the distance between the two points in a cell. The theoretical travel time, T_{ci}, from the dispatching point to a receiving point, as illustrated in Fig. 3(a), is calculated as:

$$T_{ci} = \sum s_j l_j \tag{1}$$

In which s_j is the slowness (inverse of wave velocity). Using Eq. (1), travel time is computed for all possible ray paths, and then the ray path for the first travel time and its magnitude is obtained by selecting the most reasonable ray path among the available ones. With SIRT, the difference between T_{ci}, and the observed travel time, T_{oi}, is calculated using the following equation and then distributed among all cells intercepted by the ray path.

$$\Delta T_i = T_{oi} - T_{ci} \tag{2}$$

The distribution is conducted with the lengths of the ray paths as the weights, as shown in the following equations:

$$S_i = \sum_j \Delta s_{ij} l_{ij} / \sum_j l_{ij}, \quad \Delta S_{ij} = \left(\sum_j \Delta T_i l_{ij}\right) / \left(\sum_j l_{ij}\right) \tag{3}$$

Wave attenuation, on the other hand, is represented by the decay of energy as it propagates through a material. The amplitude factor, F_{oi} of an observed wave propagating from the source can be written as:

$$F_{oi} = \frac{A_i}{A_o} \tag{4}$$

where A_o and A_i are amplitudes of wave at the source and receiving points, respectively. Adopting the ray-trace methodology, the theoretical amplitude factor, F_{ci}, from the dispatching point to a receiving point, (see Fig. 3(b)), can be expressed as follows:

$$F_{ci} = \prod_j e^{-\alpha_j l_j} \tag{5}$$

where α_j is the coefficient of attenuation. Eq. (6) is in a form equivalent to Eq. (1). Therefore, any ray-trace algorithm suitable for computing travel time can be employed without major modification and the difference between the observed and theoretical amplitude factor is distributed accordingly to each cell covered by the ray path using SIRT methodology

$$\Delta F_i = F_{oi} - F_{ci} = \sum_j \frac{\partial F_{ci}}{\partial \alpha_j} \Delta \alpha_{ij} \tag{6}$$

Similar procedure for iterative computation can be carried out to solve this nonlinear problem. The result is expressed as the attenuation coefficient for each cell, which can then be inverted to obtain amplitude factor that characterizes the soundness of each cell.

A three dimensional ray-trace technique using isoparametric coordinate projections was developed by the co-authors of this current paper and its suitability for measuring large scale concrete structures has been experimentally confirmed [22]. In this algorithm, an object is subdivided into a group of hexahedral cells, which are then transformed to first-order isoparametric elements and the length of each ray path is computed by considering projection between the nodal points, n_i, of the elements. Projection from the isoparametric coordinate (ξ, η, ζ) to the global coordinate (x, y, z) can be expressed by

$$x = a_{1x}\xi + a_{2x}\eta + a_{3x}\zeta + a_{4x}\xi\eta + a_{5x}\xi\zeta + a_{6x}\eta\zeta + a_{7x}\xi\eta\zeta + a_{8x}, \tag{7}$$

$$y = a_{1y}\xi + a_{2y}\eta + a_{3y}\zeta + a_{4y}\xi\eta + a_{5y}\xi\zeta + a_{6y}\eta\zeta + a_{7y}\xi\eta\zeta + a_{8y}, \tag{8}$$

$$z = a_{1z}\xi + a_{2z}\eta + a_{3z}\zeta + a_{4z}\xi\eta + a_{5z}\xi\zeta + a_{6z}\eta\zeta + a_{7z}\xi\eta\zeta + a_{8z} \tag{9}$$
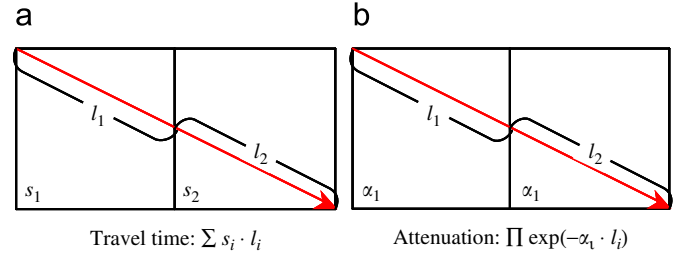
Fig. 3. Concepts of theoretical calculation for tomography reconstruction. (a) Travel time, and (b) attenuation (amplitude factor).

where a_{ix}, a_{iy} and a_{iz} ($i=1, 2, 3,\ldots, 8$) are general coefficients in x, y and z directions, respectively. Hence the coefficient can be obtained by substituting the global coordinate and the isoparametric coordinate of n_i to Eqs. (7)–(9). In the case for x direction, for example, the computation can be represented in the following matrix form:

$$\begin{bmatrix} x_1 \\ x_2 \\ x_3 \\ x_4 \\ x_5 \\ x_6 \\ x_7 \\ x_8 \end{bmatrix} = \begin{bmatrix} -1 & -1 & -1 & 1 & 1 & 1 & -1 & 1 \\ 1 & -1 & -1 & -1 & -1 & 1 & 1 & 1 \\ 1 & 1 & -1 & 1 & -1 & -1 & -1 & 1 \\ -1 & 1 & -1 & -1 & 1 & -1 & 1 & 1 \\ -1 & -1 & 1 & 1 & -1 & -1 & 1 & 1 \\ 1 & -1 & 1 & -1 & 1 & -1 & -1 & 1 \\ 1 & 1 & 1 & 1 & 1 & 1 & 1 & 1 \\ -1 & 1 & 1 & -1 & -1 & 1 & -1 & 1 \end{bmatrix} \begin{bmatrix} a_{1x} \\ a_{2x} \\ a_{3x} \\ a_{4x} \\ a_{5x} \\ a_{6x} \\ a_{7x} \\ a_{8x} \end{bmatrix} \tag{10}$$

Assuming that a ray travels in a straight path from the dispatched node to the destination node, its path can be described as follows, with x as the parameter in the global coordinate:

$$y = a_y x + b_y, \tag{11}$$

$$z = a_z x + b_z \tag{12}$$

By substituting Eqs. (7)–(9) into Eqs. (11) and (12), the transferred path can be described in isoparametric coordinate as follows

$$a_{11x}\xi + a_{12x}\eta + a_{13x}\zeta + a_{14x}\xi\eta + a_{15x}\xi\zeta + a_{16x}\eta\zeta + a_{17x}\xi\eta\zeta + a_{18x} = 0, \tag{13}$$

$$a_{21x}\xi + a_{22x}\eta + a_{23x}\zeta + a_{24x}\xi\eta + a_{25x}\xi\zeta + a_{26x}\eta\zeta + a_{27x}\xi\eta\zeta + a_{28x} = 0 \tag{14}$$

in which

$$a_{11x} = a_{1y} - a_y a_{1x}, \tag{15}$$

$$a_{12x} = a_{2y} - a_y a_{2x}, \tag{16}$$

$$a_{13x} = a_{3y} - a_y a_{3x}, \tag{17}$$

$$a_{14x} = a_{4y} - a_y a_{4x}, \tag{18}$$

$$a_{15x} = a_{5y} - a_y a_{5x}, \tag{19}$$

$$a_{16x} = a_{6y} - a_y a_{6x}, \tag{20}$$

$$a_{17x} = a_{7y} - a_y a_{7x}, \tag{21}$$

$$a_{18x} = a_{8y} - a_y a_{8x} - b_y, \tag{22}$$

$$a_{21x} = a_{1z} - a_z a_{1x}, \tag{23}$$

$$a_{22x} = a_{2z} - a_z a_{2x}, \tag{24}$$

$$a_{23x} = a_{3z} - a_z a_{3x}, \tag{25}$$

$$a_{24x} = a_{4z} - a_z a_{4x}, \tag{26}$$

$$a_{25x} = a_{5z} - a_z a_{5x}, \tag{27}$$

$$a_{26x} = a_{6z} - a_z a_{6x}, \tag{28}$$

$$a_{27x} = a_{7z} - a_z a_{7x}, \tag{29}$$

$$a_{28x} = a_{8z} - a_z a_{8x} - b_z \tag{30}$$

Because the hexahedral cell is projected to a cubic cell in the isoparametric coordinate consisting of six planes, i.e. $\xi = \pm 1$, $\eta = \pm 1$ and $\zeta = \pm 1$, the intersection point of the ray path given by Eqs. (13) and (14) in the cubic cell is obtained by substituting the equation for each plane. As example, the intersection of ray path and plane $\xi = 1$ is acquired using the following:

$$a_{11x} + a_{12x}\eta + a_{13x}\zeta + a_{14x}\eta + a_{15x}\zeta + a_{16x}\eta\zeta + a_{17x}\eta\zeta + a_{18x} = 0, \tag{31}$$

$$a_{21x} + a_{22x}\eta + a_{23x}\zeta + a_{24x}\eta + a_{25x}\zeta + a_{26x}\eta\zeta + a_{27x}\eta\zeta + a_{28x} = 0 \tag{32}$$

Eqs. (31) and (32) can be rewritten in the following forms:

$$\eta + \frac{c_{13}\zeta}{c_{11} + c_{12}\zeta} + \frac{c_{14}}{c_{11} + c_{12}\zeta} = 0, \tag{33}$$

$$\eta + \frac{c_{23}\zeta}{c_{21} + c_{22}\zeta} + \frac{c_{24}}{c_{21} + c_{22}\zeta} = 0 \tag{34}$$

in which

$$c_{11} = a_{12x} - a_{14x}, \tag{35}$$

$$c_{12} = a_{16x} - a_{17x}, \tag{36}$$

$$c_{13} = a_{13x} - a_{15x}, \tag{37}$$

$$c_{14} = a_{18x} - a_{11x}, \tag{38}$$

$$c_{21} = a_{22x} - a_{24x}, \tag{39}$$

$$c_{22} = a_{26x} - a_{27x}, \tag{40}$$

$$c_{23} = a_{23x} - a_{25x}, \tag{41}$$

$$c_{24} = a_{28x} - a_{21x} \tag{42}$$

A quadratic equation can be obtained from Eqs. (33) and (34), as given below:

$$(c_{13}c_{22} - c_{12}c_{23})\zeta^2 + (c_{13}c_{21} + c_{14}c_{22} - c_{12}c_{24} - c_{11}c_{23})\zeta$$
$$+ c_{14}c_{21} - c_{11}c_{24} = 0 \tag{43}$$

Eq. (43) can be solved as follows:

$$\zeta = \frac{-C_2 \pm \sqrt{C_2{}^2 - 4C_1 C_3}}{2C_1} \tag{44}$$

where

$$C_1 = c_{13}c_{22} - c_{12}c_{23}, \tag{45}$$

$$C_2 = c_{13}c_{21} + c_{14}c_{22} - c_{12}c_{24} - c_{11}c_{23}, \tag{46}$$

$$C_3 = c_{14}c_{21} - c_{11}c_{24} \tag{47}$$

Eq. (44) provides two solutions at a maxima because a straight line in the global coordinate becomes curving in the isoparametric coordinate. Therefore, only the solutions of $-1 \leq \zeta \leq 1$ and $-1 \leq \eta \leq 1$ are considered as the intersection point of the ray path and a specific element. Furthermore, when C_1 is found to be zero or the equation has complex solution, implication can be made in such way that ray path does not make contact on the surface at one point, i.e. intersection point does not exist, since the ray path can be assumed to be in parallel to the surface of the specific element.

In order to obtain the length of ray path, it becomes necessary to transfer the coordinates of intersection point from the isoparametric coordinates to the global coordinates. If a projection intercepts a cell in a nonlinear manner and the length of path cannot be solved directly using Eqs. (7)–(9), the Newton–Raphson method is adopted as an additional procedure to obtain the coordinates of the centre point and then estimate its length. After that, the length of individual ray path can be substituted into Eq. (1) to find the theoretical travel time, or in Eq. (4) for calculating theoretical amplitude factor. Although the elaborated algorithm is basically applicable to both techniques, a different configuration is applied for ray-tracing in the attenuation tomography so that the length of ray path is determined based on the shortest possible ray path from dispatching to receiving point, instead of the shortest travel time as adopted for the travel-time tomography.
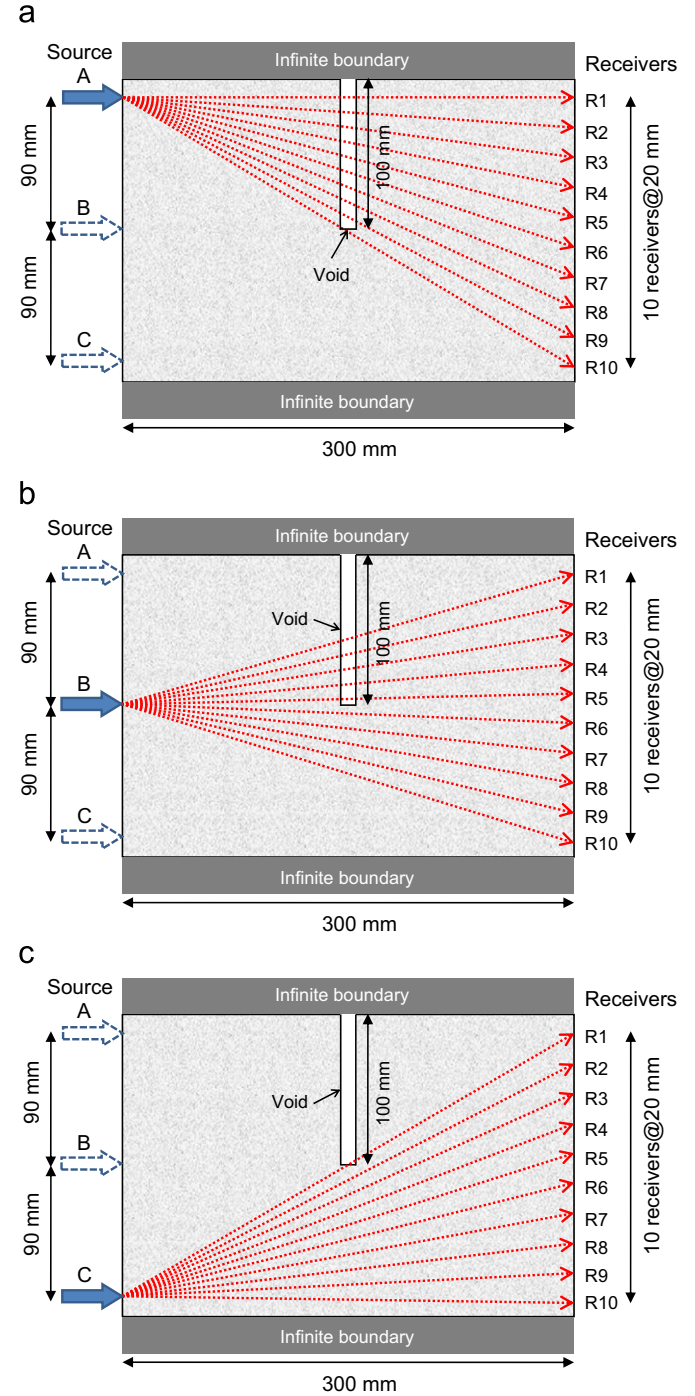

Fig. 4. Simulation of ultrasound propagation from different source locations. (a) Source location A, (b) source location B, and (c) source location C.

## 4. Simulation of ultrasound attenuated by defect

4.1. Model

To investigate the sensitivity of ultrasound attenuation towards anomaly, numerical simulations of wave motion was carried out using a commercially available software [23], which is formulated for solving two-dimensional elastic wave propagation problems using the finite difference approach [24]. As shown in Fig. 4, the simulation model was a 300×200 mm^2 area that represented concrete. A void of 100×5 mm^2 extended from the top centre of the model and downwards was included to represent a crack. The general geometry and dimensions of the model were determined in a way to resemble the experimental conditions, which are discussed in detail in the following section.

The relevant properties used for modelling wave propagation in concrete material were as follows: density of 2300 kg/m^3; the first and second Lame constants of 10 and 15 GPa, respectively. The defined parameters resulted in a longitudinal wave velocity of 4170 m/s. Damping parameters were not defined in this simulation to neglect the effect of energy loss due to heat absorption. Infinite boundary conditions were defined for the top and bottom sides of the model as to avoid any reflection which could interfere with the forward propagating wave. A model without crack was also prepared with the same geometry and material properties to simulate wave propagation in the sound concrete medium.

It is known that any form of inhomogeneity will cause refraction, reflection and scattering of ultrasonic waves to occur and result in distortion of transmitted energy. In order to clarify the extend of amplitude variations due to different types of anomalies, another simulation model with a steel inclusion of similar dimensions replacing the void at the same location was prepared. The steel inclusion has a density of 7900 kg/m; the first and second Lame constants of 113.2 and 80.9 GPa, respectively, resulting in a longitudinal wave velocity of 5900 m/s. The simple model might not accurately represent the actual case of steel-reinforced concrete, instead it was considered as a comparison to investigate the variation of ultrasonic wave amplitude due to steel, a material with acoustic impendence higher than concrete, as to address the possibility of using amplitude decay for differentiating a defect in the form of void from a steel reinforcement.

In all the models, a single-cycle ultrasonic wave with a central frequency of 110 kHz was excited by placing the source at three different locations (A, B and C, respectively), as shown in Fig. 4. It is noted that source locations A and C were 10 mm from the top and bottom of model. Ten receivers with surface contact length of
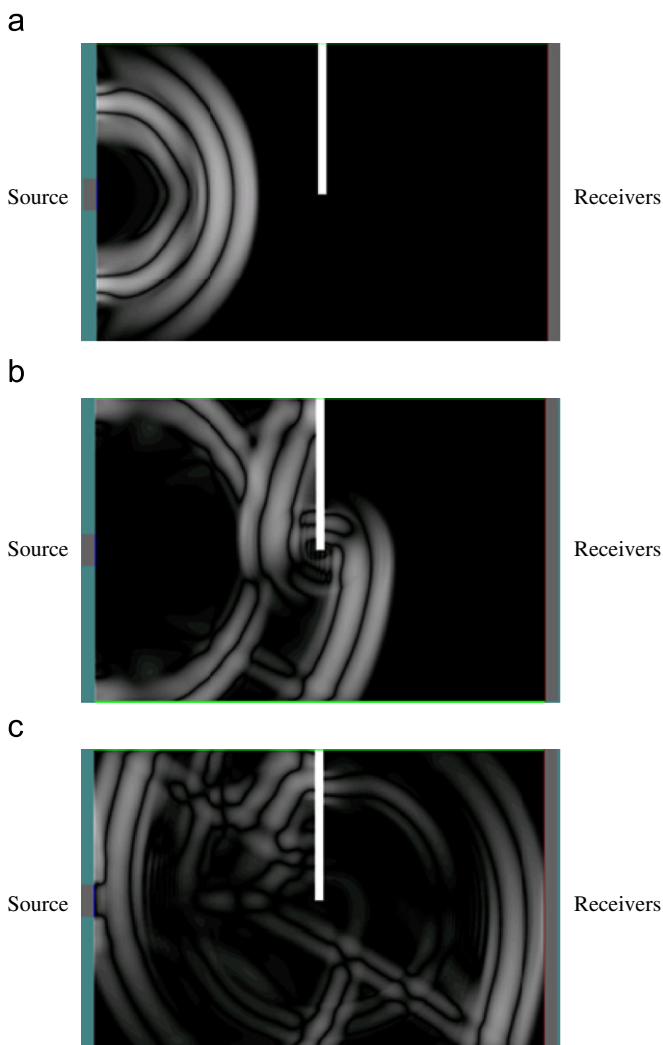
Fig. 5. Three consecutive snapshots of the simulated transient displacement field in model containing a void. (a) Wave propagating from source, (b) wave reflected, diffracted and scattered by void, and (c) wave-front reaching receiver array.
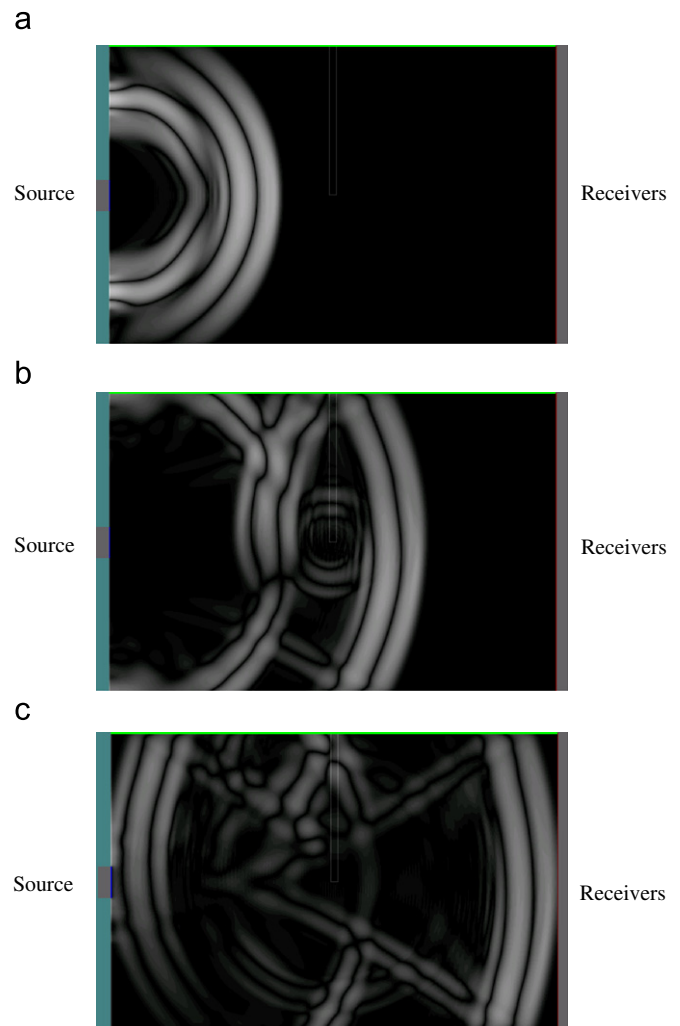
Fig. 6. Three consecutive snapshots of the simulated transient displacement field in model containing a steel inclusion. (a) Wave propagating from source, (b) wave reflected, diffracted and scattered by void, and (c) wave-front reaching receiver array.

a

b

c
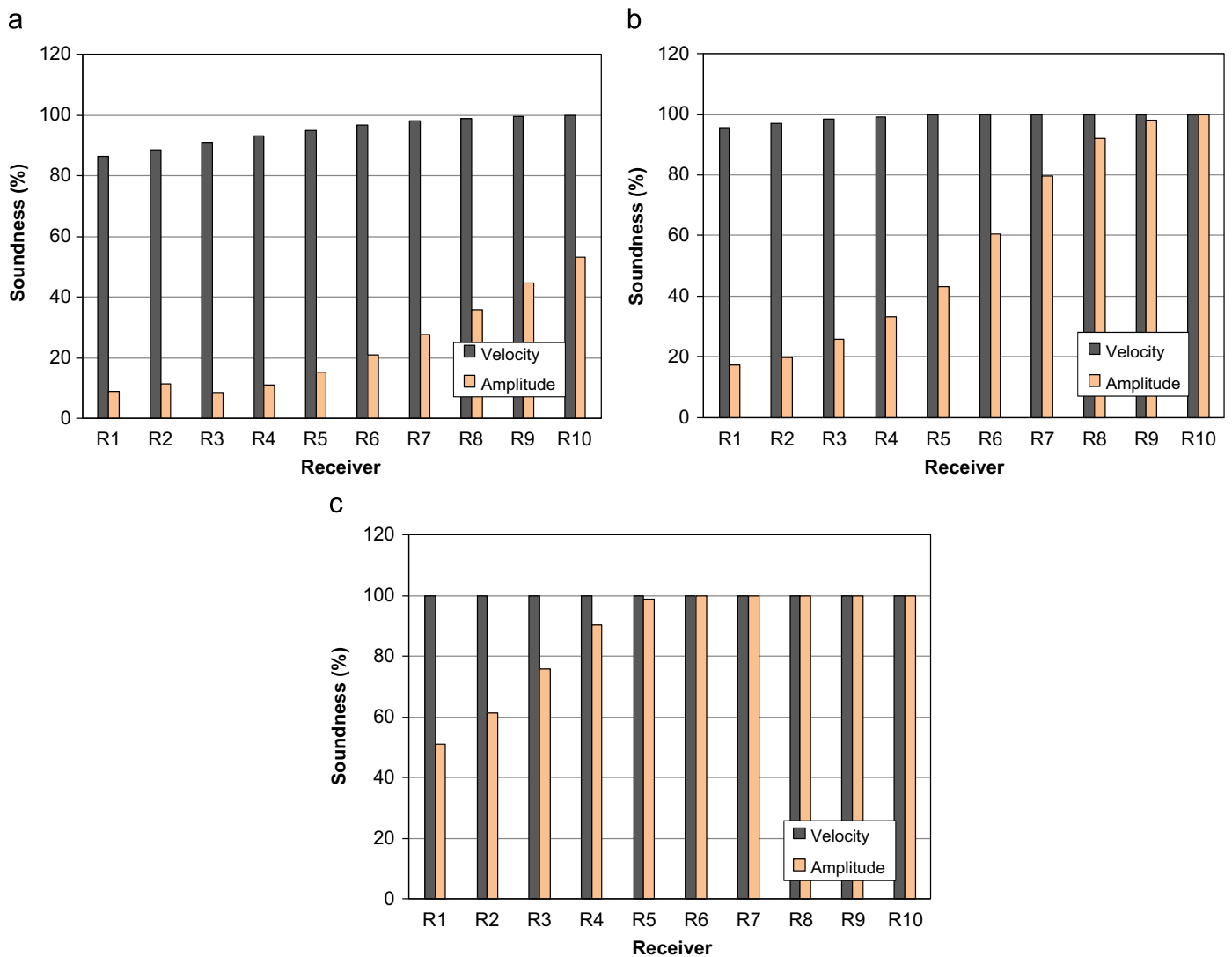
Fig. 7. Soundness of simulation model containing air void as evaluated by velocity and amplitude change for each source-receiver combination. (a) Source location A, (b) source location B, and (c) source location C.

20 mm were placed on the opposite side to record transmitted waveform at uniform centre-to-centre spacing of 20 mm. Fig. 4 also indicates the shortest ray paths from each source location to the respective receivers under the sound concrete condition. The simulation was configured by setting the spacing resolution as 0.58 mm, which was considered sufficient, since the estimated wavelength was 38 mm at a P-wave velocity of 4170 m/s. This resulted in 65 points per wavelength, while in the time domain a duration equalled to the nominal period of the wave was represented by 60 points, which were more than sufficient considering that 20 points per wavelength and period were considered satisfactory for similar simulations of elastic waves [25].

4.2. Results

Wave motions as observed during the simulation of model with void are given in Fig. 5, showing the transmission of ultrasound from source location B. The wave was diffracted and scattered by the void before reaching the receiver array on the opposite side of model. (see Fig. 5(b)). Delay in travel time for ray paths blocked by the void could be noticed in the simulation. In addition, the wave

amplitudes were lower because some of the wave energy did not reach the receivers.

The propagation of ultrasound in the model with steel inclusion is shown in Fig. 6. It was clearly seen that although part of the wave energy was diffracted and scattered at interface between concrete and steel, some has transmitted into the steel as a result of higher acoustic impedance of steel compared to concrete, as shown in Fig. 6(b). Due to the direct transmission, the wave front of ultrasound experienced no delay in reaching the receivers; conversely faster propagation could be anticipated because of the higher propagation velocity in steel compared to concrete.

To quantitatively compare the sensitivity of velocity and amplitude change with regard to void and steel inclusion, the soundness of each model was evaluated from the data of each ray path. The soundness is expressed as the percentage of velocity or amplitude of waves as received by each sensor in the model containing inhomogeneity (void or steel inclusion) with reference to those in the sound model. Thus, the soundness value is always 100% for ray path in the homogeneous portion. As shown in Fig. 7, simulation results of the model with void confirmed that amplitude of ultrasound decreased noticeably compared to the calculated
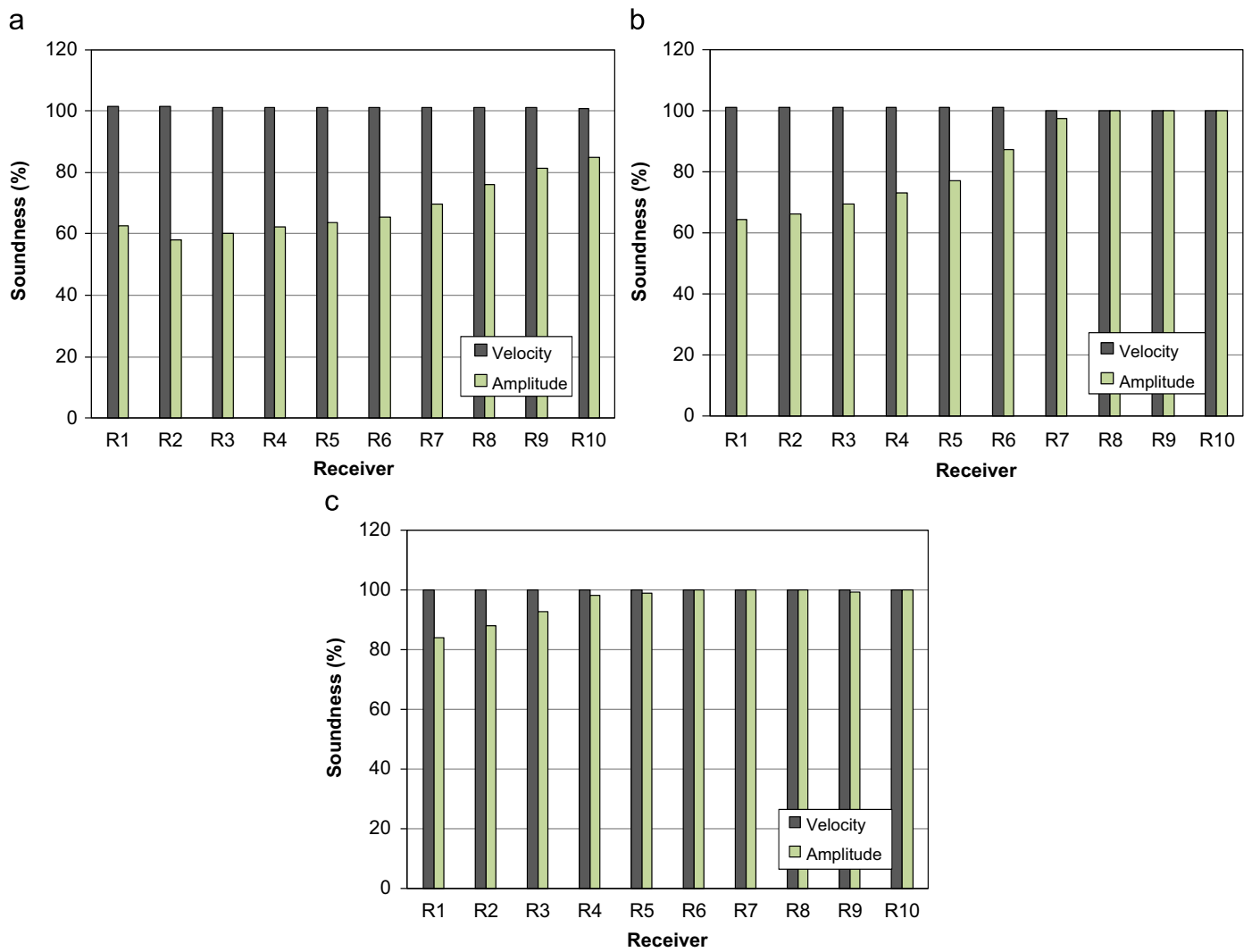
Fig. 8. Soundness of simulation model containing steel inclusion as evaluated by velocity and amplitude change for each source-receiver combination. . (a) Source location A, (b) source location B, and (c) source location C
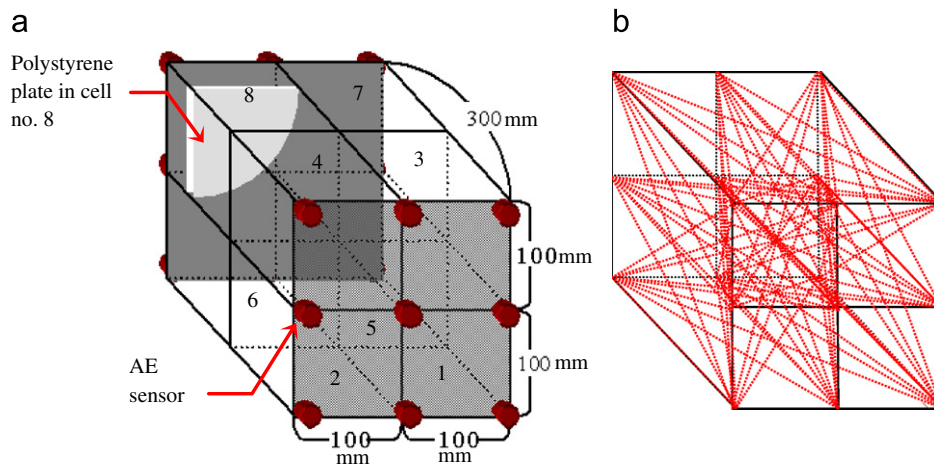

Fig. 9. Details of specimen with artificial defect. (a) Sensor arrangement and cell discritization, and (b) ray-path coverage.

velocity for ray paths blocked by the defect. In the case of results from source location A given as in Fig. 7(a), it can be seen that even for the least affected ray path, i.e. from the source to receiver R10,

amplitude has dropped to approximately half for the case of defective concrete relatively to the homogeneous concrete; whereas the velocity remained almost unchanged. In addition to

this, the results for source locations B and C indicated that ray paths which were nearby the defect but not directly affected (recorded by receivers R6 and R7 for source location B), as well as R2 and R3 for source location C, (see Fig. 7(b) and (c)) also registered decreases in amplitude of more than 30–40%, contrary to the negligible decrease in velocity for the same ray paths.

The results of simulating model with steel inclusion are given in Fig. 8. It was shown that the soundness values computed from velocity of ray paths covering the steel inclusion were approximately 1% higher compared to the sound model. The positive change was not apparent, but could increase depend upon the dimension of steel inclusion in relative to concrete. In contrast to the increase of soundness by velocity, decrease of soundness by amplitude was noted, especially for the ray paths that covered the steel inclusion, which exhibited a maximum of approximately 42% decrease as recorded by receiver R2 for source location A (see Fig. 8(a)). Although the decreases were far low compared to those acquired from the equivalent ray paths in the model with void, this nevertheless implied that the assessment using the attenuation of ultrasound should be performed with caution, since any form of inhomogeneity could possibly cause amplitude decay. It is also considered that the high sensitivity nature of attenuation, if utilized wisely could help enhance the reliability of soundness assessment of concrete structures.
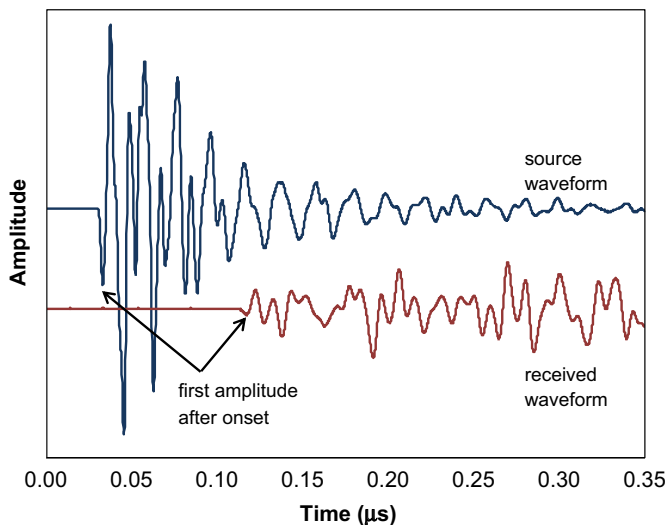
5. Measurement of three-dimensional attenuation tomography

5.1. Experiment detail

A laboratory experiment was conducted to examine the feasibility of attenuation tomography for visualizing defect in concrete. A concrete slab of $1500 \times 1500 \times 300$ mm^3 was used. Styrofoam plates of 300 mm diameter were included at specific locations. The same specimen was used for a different purpose, as reported elsewhere [26]. In order to simulate boundary free experiment, in this current study the measurements were limited to two $200 \times 200 \times 300$ mm^3 portions near the middle of the specimen, which included one quarter of the defect. This was because reflections at specimen sides potentially complicate data interpretation and impose result uncertainties. As illustrated in Fig. 9(a), the first portion contained a quarter of a 5 mm-thick circular Styrofoam plate of 300 mm in diameter, which was embedded 30 mm from and in parallel to the surface of the specimen. Due to its very low acoustic impedance compared to concrete, the Styrofoam plate was considered as a void. The second portion consisted only of homogeneous concrete in order to provide reference measurement result.

The concrete was prepared using ordinary Portland cement and limestone aggregates with maximum size of 20 mm. The specimen was cured under air after casting. The average compressive strength and static elastic modulus obtained on 28-day after casting were 29.1 MPa and 26.4 GPa, respectively.

Tomography measurements were carried out with both the measured portions discretized into 8 uniform solid cells of $100 \times 100 \times 150$ mm^3. This resulted in a total of 9 nodes on each of the two measurement surfaces, which also served as the source/receiving points. It is noted that cell no.8 was the only cell containing the artificial defect. A source-receiver system was instrumented to measure transmitted waves from one side to the opposite, using an ultrasonic pulser (PAC HV-101) as the source and 60 kHz resonant type acoustic emission (AE) sensors (PAC R6) as receivers. Ultrasonic pulses with central frequency of approximately 110 kHz were generated by the pulser at one of the node locations on one side and be received on the opposite side by nine receivers. Pulse generation and waveform recording was subsequently conducted for all the node locations on the same side before inverting the source-receiver arrangement for pulse generation from the opposite side. Ray-path coverage in the specimen is shown in Fig. 9(b). The total number of 162 measurements on both sides were recorded with a sampling time of 0.125 μs and a

Fig. 10. Example of measured source and received waveforms.
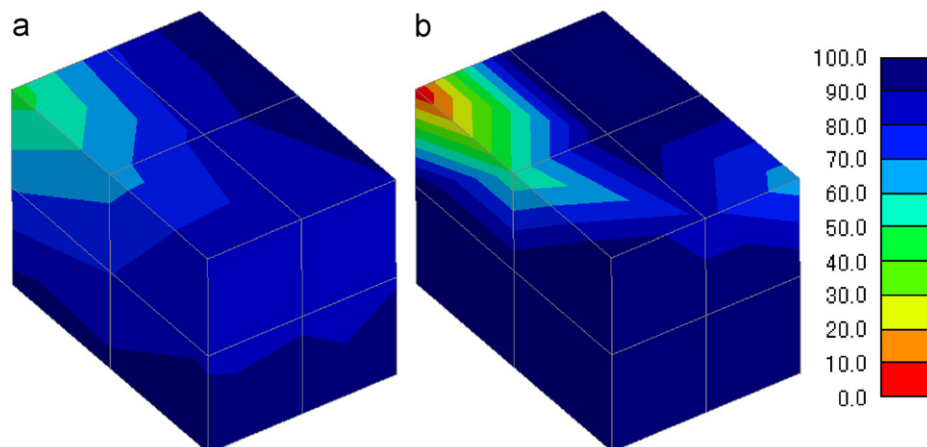

Fig. 11. Tomography visualization results for the portion containing defect (unit in % of soundness). (a) Velocity tomography and (b) attenuation tomography.

duration of 3072 samples by a multi-channel AE measurement system (PAC Mistras System).

5.2. Results and discussion

Typical waveforms of the source and receiver are shown in Fig. 10. The experimental amplitude factor, F_{oi}, was taken as the ratio between absolute magnitudes of the first cycle of the source and the receiver after onset. By plotting the amplitude factors of all the ray paths acquired from measuring the sound concrete portion against propagation distance, the coefficients of attenuation for homogeneous concrete, α_h was obtained as 5.2316 m^{-1} based on the regression analysis. The α_h value, which was employed as the initial theoretical value in computation, was assigned to each cell in the computation model to characterize initial attenuation. Computations were carried out simultaneously for all projections in the respective cells to repeatedly adjust the theoretical values of α for each cell, so that the discrepancy between the theoretical amplitude factor (computed using Eq. (5)) and the observed data for each projection could be minimized. The computation was performed for 20 iterations to achieve convergence. The assigned α values were used to calculate the unit amplitude factor, i.e. amplitude factor when ray length is 1 m, to define characteristic attenuation of ultrasound in respective cells.

For comparison, travel time was also extracted using the same measurement data to compute travel time tomography. The computation was carried out by adopting another available algorithm dedicated to the purpose. Results of computation indicated a drastic drop of 99% for cell no.8, which contained the defect. For velocity, a lesser drop of 45% was obtained for the same cell. As in the case for other cells, which contained no defect, particularly cell nos. 3, 4, 6 and 7, greater change in attenuation in relative to velocity was also noticed. The experimental results of tomography confirmed the higher sensitivity of wave attenuation compared to velocity when investigating defect in concrete. However, it should be understood in the presence of a defect, wave diffraction and scattering for paths directly blocked by the defect happened. There was possibility the backscattered energy superimposed with the incoming ones that propagated on paths not directly blocked by the defect. The superimposition could have adversely distorted the transmitted energy and resulted in decrease of amplitude. Hence, indirect decay of amplitude was likely to occur to could cause underestimation of unit amplitude factor.

Fig. 11 shows the tomography visualization results for velocity and amplitude normalized to the ratios for velocity and the unit amplitude factor. From the tomograms it can be seen that, both velocity and amplitude factor were effective in indicating the location of defect, with the attenuation tomography yielded a sharper contrast, indicating greater difference in soundness between the sound and defective region.

By studying the ray-path coverage as in Fig. 11(b), one may be aware of the presence of "blind zones", i.e. regions that were not intersected by any projected ray, particularly near the edges or boundaries of the measurement perimeter. In the actual measurement, the blind zones could only be reduced by employing a finer sensor arrangement, or by increasing the surface of access, which was, however not possible in this study. On the other hand, in the analysis each cell in the model was deemed to have contained sufficient amount of measured information (observed data offered by intersecting ray), so that the developed algorithm could perform repeated computations and adjustments until the approximation of amplitude factor for each cell by tracing simulated rays through the model was achieved with low residual error compared to the measured data.

Considering that tomography reconstruction is closely dependent upon the number and arrangement of sensors as well as mesh discretization, even though the scale and depth of the defect from concrete surface was not precisely visualized, the problematic region was effectively detected. With the finding from this experiment, it can be suggested that the attenuation tomography be used as a fast complementary technique to the travel time tomography, since it can serve to increase the creditability of assessment by only changing the analysis method of data, without having to conduct additional measurement. The high sensitivity of attenuation is considered capable to provide a better visualization for inhomogeneity, hence could help improve detection and characterization of defect when used as a cross-reference with the travel-time tomography. Further study is focused on issues relating to optimizing the measurement instrumentation as well as model construction. Furthermore, to realize on-site measurement of existing structures in large scale, appropriate instrumentation for adoption of high energy, low frequency waves is worth taken into account.

6. Conclusion

As indicated by the fundamental experimental results and numerical simulations, the amplitude of ultrasound propagating in concrete undergoes a much greater change compared to the delay in travel time due to inhomogeneity. This characteristic underlines the high sensitivity of ultrasound attenuation for potential adoption in technique for evaluating soundness of concrete. To realize this, an attenuation tomography reconstruction technique using a three-dimensional ray-trace algorithm was developed and its feasibility was examined experimentally using a large concrete specimen instigated with an artificial defect. The same set of measurement data was used to extract information on travel time and amplitude decay of ultrasound for the travel time and attenuation tomography reconstruction procedures, respectively. The attenuation tomography result was comparable to the travel time tomography result in effectively visualizing the location of defect embedded in concrete, suggesting the usefulness of the technique as a complementary method for verifying the results of travel time tomography, under the convenient condition that no additional measurement was necessary. It should be noted that, apart from cracks, any other form of anomaly, e.g steel reinforcement also causes attenuation up to a certain extent, as indicated by the simulation results. Furthermore, micro-structural aspects in concrete (aggregates, sand grains, pores, etc.) also influenced the overall attenuation. However, any measurement scatter is insufficient to mask the clear decrease of the amplitude by at least one order of magnitude due to the presence of defect that possessed much lower acoustic impedance, as such no significant ultrasound energy could be transmitted.

Reference

[1] Bond LJ, Kepler WF, Frangopol DM. Improve assessment of mass concrete dams using acoustic travel time tomography. part I- theory. Constr. Build. Mater. 2000;14:133–46.

[2] Kocur GK, Saenger EH, Vogel T. Elastic wave propagation in a segmented X-ray computed tomography model of a concrete specimen. Constr. Build. Mater. 2010;24:2393–400.

[3] Suzuki T, Ogata H, Takada R, Aoki M, Ohtsu M. Use of acoustic emission and X-ray computed tomography for damage evaluation of freeze-thawed concrete. Constr. Build. Mater. 2010;24:2347–52.

[4] Kase E, Ross T. Using seismic tomography and holography ground imaging to improve site investigation. Proc. No-Dig, New Orleans, 2004: Paper C-4-02. Constr. Build. Mater. 2010;24:2393–400.

[5] Zhou C, Liu L, Lane Jr JW. Nonlinear inversion of borehole–radar tomography data to reconstruct velocity and attenuation distribution in earth materials. J. Appl. Geophys. 2001;47:271–84.

[6] Luxbacher K, Westman E, Swanson P, Karfakis M. Three-dimensional time-lapse velocity tomography of an underground longwal panel. Int. J. Rock Mech. Min. Sci. 2008;45(4):478–85.

[7] Jackson MJ, Tweeton DR. MIGRATOM—Geophysical tomography using wave-front migration and fuzzy constraints. Report of Investigation, R.I. 9497. United States Department of Interior: Bureau of Mines; 1993. 35 p.

[8] Martin J, Broughton KJ, Giannopolous A, Hardy MSA, Forde MC. Ultrasonic tomography of grouted duct post-tensioned reinforced concrete bridge beams. NDT&E Int. 2001;34:107–13.

[9] Liu L, Guo T. Seismic non-destructive testing on a reinforced concrete bridge column using tomographic imaging techniques. J. Geophys. Eng. 2005;2:23–31.

[10] Kepler WF, Bond LJ, Frangopol DM. Improved assessment of mass concrerte dams using acoustic travel time tomography. part II—application. Constr. Build. Mater. 2000;14:147–56.

[11] Aggelis DG, Shiotani T. Repair evaluation of concrete cracks using surface and through-transmission wave measurements. Cem. Concr. Compos. 2007;29:700–11.

[12] Shiotani T, Aggelis DG, Momoki S. Damage evaluation of concrete structures by seismic tomography. Tobishima Tech. Rep. 2007;56:111–6. [in Japanese].

[13] Shiotani T, Aggelis DG. Evaluation of repair effect for deteriorated concrete piers of intake dam using AE activity. J. Acoust. Emission. 2007;69–79.

[14] Miyanaga T, Kuroki H, Momoki S. Evaluating repair effect of concrete structures by three-dimensional elastic wave tomography. Electr. Power Civil Eng. 2010;345:16–20. [in Japanese].

[15] Shiotani T, Momoki S, Chai HK, Aggelis DG. Elastic wave validation of large concrete structures repaired by means of cement grouting. Constr. Build. Mater. 2009;23(7):2647–52.

[16] Best AI, McCann C, Sothcott J. The relationships between the velocities, attenuations, and petrophysical properties of reservoir sedimentary rocks. Geophys. Prospect. 1994;42:151–78.

[17] Brzostowski M, McMechan G. 3-D tomographic imaging of near-surface seismic velocity and attenuation. Geophysics 1992;57:396–403.

[18] Quan Y, Harris M. Seismic attenuation tomography using the frequency shift method. Geophysics 1997;62(3):895–905.

[19] Huang Z, Huang L, Miao L. Study on computerized tomography of ultrasonic attenuation for concrete. J. Railw. Sci. Eng. 2004;1(2):35–8. [in Chinese].

[20] Aggelis DG, Shiotani T. Effect of inhomogeneity parameters on wave propaga-tion in cementitious material. ACI Mater. J. 2008;105(2):187–93.

[21] Sassa K. Suggested methods for seismic testing within and between boreholes. Int. J. Rock Mech. Min. Sci. Geomech. Abstr. 1988;25(6):449–72.

[22] Kobayashi Y, Shiotani T, Aggelis DG, Shiojiri H. Three-dimensional seismic tomography for existing concrete structures. Proc. Second Int. Operational Modal Analy. Conf., Copenhagen Apr 2007;2:595–600.

[23] Wave2000, Cyber-Logic, Inc., NY, ⟨http: www.cyberlogic.org⟩.

[24] Luo G, Kaufman JJ, Chiabrera A, Bianco B, Kinney JH, Haupt D, Ryaby J, Siffert RS. Computational methods for ultrasonic bone assessment. Ultrasound Med. Biol. 1999;25(5):823–30.

[25] Moser F, Jacobs LJ, Qu J. Modeling elastic wave propagation in waveguides with finite element method. NDT&E Int. 1999;32:225–34.

[26] Chai HK, Aggelis DG, Momoki S, Kobayashi Y, Shiotani T. Single-side access tomography for evaluating interior defect of concrete. Constr Build. Mater. 2010;24(12):2411–8.